Geophys. J. Int. (2004) **156,** 222–236 doi: 10.1111/j.1365-246X.2003.02107.x

Scattering of elastic waves in heterogeneous media using the direct solution method

Ursula Iturrarán-Viveros,[1] Francisco J. Sánchez-Sesma[2] and François Janod[2]

[1] *Instituto Mexicano del Petróleo, Eje Central Lázaro Cárdenas* 152, *CP* 07730, *México DF, Mexico. E-mail: uiturrar@imp.mx*
[2] *Instituto de Ingeniería, UNAM, Cd. Universitaria, Apdo* 70-472, *Coyoacán CP* 04510, *México DF, Mexico. E-mail: sesma@servidor.unam.mx*

Accepted 2003 August 11. Received 2003 July 28; in original form 2002 February 18

SUMMARY

Multiple scattering is a phenomenon generic to wave propagation in heterogeneous media. In order to study scattering effects caused by inhomogeneities within an elastic medium we use the *direct solution method* (DSM). This method is based on solving the weak form of the elastic equation of motion. A complete set of trigonometric functions is used as trial functions to study 2-D problems. The computational costs of this method increase with frequency. To partially overcome this problem we use the discrete fast Fourier sine/cosine transforms. One of the problems that arises in the application of discrete solution methods for wave propagation calculations is the presence of reflections from the boundaries of the numerical mesh. We apply absorbing boundary conditions at the edges and corners. We use the stiffness concept for a three-quarter-space (calculated using the indirect boundary element method) to reduce the undesirable reflected waves generated at the corners. We also apply the stiffness concept for a quarter-space to impose free-surface boundary conditions. We consider *SH*-wave propagation (incident plane waves and line sources) in a 2-D space with natural boundary conditions. Comparisons with analytical solutions for simple problems are shown.

Key words: Fourier transforms, inhomogeneous media, lateral heterogeneity, numerical techniques, scattering.

1 INTRODUCTION

Scattering of seismic waves plays a significant role in seismic wave propagation in the Earth. Phenomena such as coda-wave excitation, attenuation and irregular arrival times are often assumed to be caused by scattering from inhomogeneities in the crust and upper mantle of the Earth. The study of sound wave propagation through highly heterogeneous media is useful to understand information provided by acoustic waveform logs and will have a direct impact in oil production. The Earth is not a homogeneous body and this has stimulated seismologists to study scattered waves to explain some of the features they observe on seismograms. The Earth has heterogeneities on many scales and it is mandatory to account for this fact. An excellent overview of theoretical aspects of scattering and the influence of small- and large-scale heterogeneities on wave fronts travelling through heterogeneous media can be found in Sato & Fehler (1998).

A great variety of approaches are available in the literature. It is worth mentioning the approach due to Virieux (1984) where the author simulated *SH*-wave propagation in a salt dome inside a two-layered medium using a finite-difference method (FDM) in terms of velocity and stresses. Also using FDM, Frankel & Clayton (1986) studied scattering of elastic and acoustic waves in 2-D media with random spatial variations. A numerical study of coda Q in two-layer random media is presented in Yomogida *et al.* (1997) applying a boundary integral scheme. The T-matrix approach is used in Varadan *et al.* (1989) to study scattering of elastic or viscoelastic inclusions. This rapid passage over relevant approaches to simulate wave propagation in complex media gives us a glimpse of the many possibilities available. All of them have advantages and limitations. It is not our attempt to chose the best technique because there is not such a thing. Models and methods are appropriate to deal with one limited parcel of reality. Instead we centre our attention on *SH*-wave propagation in heterogeneous media using the direct solution method (DSM). The DSM is a Galerkin weak form realization of the method of weighted residuals (MWR). It is based on solving the weak form of the elastic equation of motion. The DSM is so named because the solution is obtained by directly solving a system of linear equations. The method was originally formulated for global-scale studies and only free-surface boundary conditions were considered. Geller & Ohminato (1994) computed synthetic seismograms in 2-D configurations. They imposed at the bottom of their model exact energy-absorbing boundary conditions as natural boundary conditions. Hara *et al.* (1993), Cummins (1994) and Cummins *et al.* (1997) used the DSM to compute surface wave synthetics and the partial derivatives for a laterally heterogeneous Earth model in spherical coordinates.

The objectives of this paper are as follows.

(1) To explore the applicability of the DSM with Cartesian coordinates using a complete basis of cosines as trial and weight

functions to deal with 2-D non-homogeneous media. The trial functions are used along horizontal and vertical directions. In this way the trial functions are well suited to modelling heterogeneities in both directions.

(2) To use the discrete fast cosine/sine Fourier Transforms to speed up the method.

(3) To apply the stiffness matrix for a three-quarter-space, improving absorbing boundary conditions cutting down undesirable contamination from the corners.

(4) To apply the stiffness matrix for a quarter-space to impose free-boundary conditions.

We consider heterogeneities with a size comparable to the dominant wavelength. In order to ensure a reasonable computational cost, the wavelengths have to be in a range between the size of the model and a few hundredths of it.

The simulation of wave propagation by finite-difference or finite-element methods in unbounded domains requires a specific treatment for the boundaries of the necessarily truncated computational domain. One method for eliminating undesirable reflections is creating a large and/or expanding grid. Another approach is to make the grid boundary transparent to outgoing energy. This is ideally done by designing absorbing or non-reflecting boundaries, which are mathematically equivalent to a one-way, or outgoing, elastic wave equation only. Perhaps the simplest example of absorbing boundaries comes from the application of a paraxial (one-way) wave equation at the artificial grid boundary. This method was first used by Clayton & Engquist (1977) and is limited to a range of incidence angles within which it works properly. Higdon (1990) developed an approximation of the absorbing boundary condition that is based on the composition of simple first-order differential operators. Each operator gives perfect absorption for a plane wave impinging on the boundary at a certain incidence angle. In practice, an outgoing elastic wave equation is an approximation since the wave equation is not generally separable in outgoing and incoming parts. Minimizing the coefficient of reflection at the artificial boundary is another popular technique such as in Peng & Toksöz (1994, 1995). Absorbing layers have been used in the past (see Kosloff & Kosloff 1986) with reasonable results in time-domain computations. An extension of this idea, the perfect matched layer (PML) is being used with success in finite-difference studies (e.g. Bérenger 1994; Collino & Tsogka 2001). This work deals with the DSM, thus we will remain in the frequency domain and impose absorbing boundary conditions as natural boundary conditions using the local wavenumber. Generally speaking, the absorbing boundary condition can be regarded as a linear relationship between tractions and displacements along an interface. Such an operator is called the stiffness of the interface in engineering practice (e.g. Kausel 1992). We use the indirect boundary element method (IBEM) to compute the stiffness in two canonical cases: the three-quarter-space and a quarter-space with a free boundary. These conditions allow one to reduce spurious reflections produced at the corners of the computational domain, and to impose nearby free-surface boundary conditions, respectively.

In Section 2 we discuss the feasibility of the DSM by solving a simple 1-D layered medium problem. We compare the solutions obtained using the DSM with those obtained by using the Thomson–Haskell propagator matrix method. We show the advantages of using cosine functions as trial functions, since the discrete cosine/sine fast Fourier transforms (FFTs) can be used to speed up computation. We also give indications concerning the choice of the parameters in the model and the accuracy limits. In Section 3 we give the explicit Galerkin weak form operator for the 2-D case. We briefly discuss how to compute the stiffness matrix and how its use reduces parasitic reflections generated at the corners. The stiffness concept has been applied for a quarter-space where we impose a free-surface boundary condition. In this example we consider a rectangular prominence over a half-space subjected to an incident plane wave. We discuss the advantages and disadvantages of using the stiffness formulation. In Section 4 we give comparisons between analytical solutions and results obtained using the DSM for two simple 2-D problems. The first problem is a homogeneous medium with an impulsive line source, the analytical solution is given by the Green's function. The second problem is an elastic medium with a cylindrical elastic inclusion, under incidence of a plane wave. Finally, in a last example we study the scattering effects produced by interaction of the travelling waves encountering four elastic cylinders.

2 THE DIRECT SOLUTION METHOD FOR THE 1-D CASE

The considerable variability of material properties in the near-surface part of the Earth means that a horizontally stratified model necessarily has a local meaning. In fact, a reservoir is made up of layered sedimentary rock which took shape after a long period of sedimentation and millions of years of diagenesis. Thus, a simple but reasonably realistic stack of homogeneous isotropic layers overlaying a homogeneous half-space represents the inhomogeneous medium. In this section we first consider a 1-D layered medium (Fig. 1) and show how the DSM can be used to find displacements in the domain of interest under an incident plane wave. Assuming harmonic motion, the unknown displacement v is as follows:

$$v(z) = v^{(0)}(z) + V(z), \tag{1}$$

where $v^{(0)}$ is a known driving field given by

$$v^{(0)} = v_0(\omega)\mathrm{e}^{+ik_z z}, \tag{2}$$

where the vertical wavenumber is given by $k_z = \frac{\omega}{\beta(H)}\cos\gamma$ and $v_0(\omega)$ is the reference field, with $\beta(z)$ being the velocity of shear waves at z (in this case we consider $\beta(H)$ the shear wave velocity in the half-space) and γ the incident angle. The time–horizontal space dependence is given by the factor $\mathrm{e}^{i\omega t - ik_x x}$ (where $k_x = \frac{\omega}{\beta(H)}\sin\gamma$ is the constant horizontal wavenumber), which is omitted hereafter. The function $V(z)$ is a function of depth represented as a linear combination of trial functions,

$$V(z) = \sum_{n=0}^{2N-1} c_n \phi^n(z), \tag{3}$$

where $2N$ is the number of trial functions along the z direction. The expansion coefficients c_n are the unknowns and ϕ^n are the set of trial functions. Observe that we consider the displacement v in eq. (1) as a series of trial functions plus a driving field eq. (2), which represents a plane wave. Apart from this slight difference we follow the derivations given in Geller & Ohminato (1994) and Geller & Takeuchi (1995). If an antiplane stress field is applied on a direction parallel to the y-axis, the 1-D strong form of the method of weight residuals (MWR) for the elastic equation of motion, in Cartesian coordinates, in the spectral domain (ω, k_z, z) is given by

$$\int_0^H \xi^m \left\{\rho\omega^2(v^{(0)} + V) + \frac{d}{dz}\left[\mu\frac{d(v^{(0)} + V)}{dz}\right]\right\} dz = 0, \tag{4}$$

where v is the particle displacement in the y-direction given in eq. (1), ρ is the density, μ is a Lamé constant corresponding to the shear modulus (these parameters are depth-dependent), ω is the

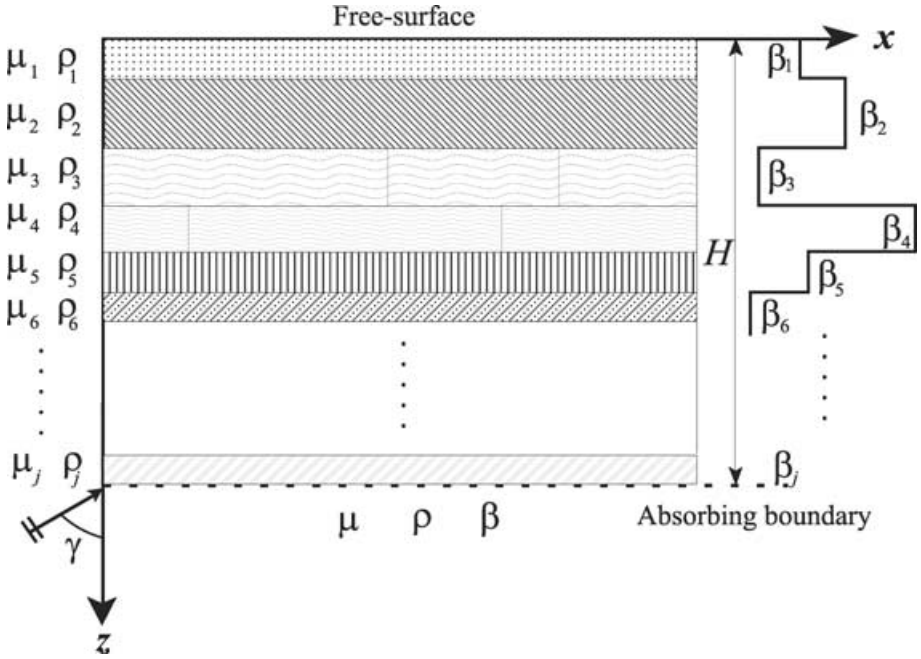

Figure 1. Layered medium subjected to an incident plane wave with an angle γ. The model is infinite along the x-axis. Elastic parameters are the density ρ_i, the shear modulus μ_i and the S-wave velocity, denoted by β_i. These three parameters are functions of depth only. The parameters for the half-space are denoted by ρ, μ and β. The boundary conditions are at $z = 0$, a free-surface boundary condition and at $z = H$, an absorbing boundary condition.

angular frequency and ξ^m are the weight functions. On the other hand, when we consider the weak form of the equation of motion we take ψ^n instead of ϕ^n in eq. (3) as follows:

$$\psi^n(z) = \begin{cases} \cos\left(\dfrac{n\pi z}{H}\right), & 0 \le n \le N-1, \\ \sin\left[\dfrac{(n-N+1)\pi z}{H}\right], & N \le n \le 2N-1, \end{cases} \tag{5}$$

where H is the size of the model along z. Then the weak form is given by

$$\begin{aligned} \omega^2 \int_0^H \psi^m \rho V \, dz - \int_0^H \frac{d\psi^m}{dz} \mu \frac{dV}{dz} \, dz - (\psi^m i k_z \mu V)_{z=H} \\ = -\omega^2 \int_0^H \psi^m \rho v^{(0)} \, dz + \int_0^H \frac{d\psi^m}{dz} \mu \frac{dv^{(0)}}{dz} \, dz \\ - \left(\psi^m \mu \frac{dv^{(0)}}{dz}\right)_{z=H} \quad (m = 0, \ldots, M-1). \end{aligned} \tag{6}$$

Note that in the weak form we are using trial and weight functions as the same set of trigonometric functions. The requirement for the existence of the integrals in eq. (6) is that both the solution v and the weight functions ψ must be continuous, but no continuity requirements are placed on the derivatives of these functions. The equivalence between the strong and weak solutions of partial differential equations is a well-known result (see Strang & Fix 1973, pp. 10–13). Following Geller & Ohminato (1994) let us integrate eq. (6) by parts to obtain eq. (4). Eq. (4) shows that natural boundary conditions for the weak form operator are:

$$\mu \frac{d(v^{(0)} + V)}{dz} = 0, \quad z = 0 \quad \text{free-surface BC} \tag{7}$$

$$\mu \frac{dV}{dz} = -ik_z \mu V, \quad z = H \quad \text{absorbing BC}. \tag{8}$$

Eq. (6) can be written in matrix form as follows:

$$(\omega^2 \mathbf{T} - \mathbf{H} + \mathbf{R})\mathbf{c} = -(\omega^2 \mathbf{T}^0 - \mathbf{H}^0 + \mathbf{R}^0), \tag{9}$$

where $\mathbf{T}$ is the kinetic energy matrix, $\mathbf{H}$ is the potential energy matrix and $\mathbf{R}$ the matrix operator that includes the natural boundary conditions. The superscript '0' represents the matrices where the incident or reference field $v^{(0)}$ (or its derivative) is involved. The explicit matrix and vector elements for the *SH* case are given by

$$T_{mn} = \int_0^H \psi^m \rho \psi^n \, dz, \quad T_m^0 = \int_0^H \psi^m \rho v^{(0)} \, dz \tag{10}$$

$$H_{mn} = H_{mn}^{(1)} + H_{mn}^{(2)}, \quad H_m^0 = H_m^{0(1)} + H_m^{0(2)}, \tag{11}$$

where

$$H_{mn}^{(1)} = \int_0^H \psi^m \mu \psi^n \, dz, \quad H_m^{0(1)} = \int_0^H \psi^m \mu v^{(0)} \, dz \tag{12}$$

$$H_{mn}^{(2)} = \int_0^H \frac{d\psi^m}{dz} \mu \frac{d\psi^n}{dz} \, dz, \quad H_m^{0(2)} = \int_0^H \frac{d\psi^m}{dz} \mu \frac{dv^{(0)}}{dz} \, dz \tag{13}$$

$$R_{mn} = -ik_z \psi^m(H) \mu(H) \psi^n(H) \tag{14}$$

$$R_m^0 = ik_z \psi^m(H) \mu(H) v^{(0)}(H). \tag{15}$$

The next step is to compute the integrals and to solve a linear system of equations to obtain the unknown coefficients in eq. (3). We will use the DCT and the DST to compute integrals in eqs (10), (12) and (13). In order to simplify computations we note that for the particular case of having the free surface at $z = 0$ the set of trial functions (5) can be replaced by

$$\psi^n(z) = \cos\left(\frac{n\pi z}{H}\right) \quad \text{and} \quad V(z) = \sum_{n=0}^{N-1} c_n \psi^n(z), \tag{16}$$

where N is the number of trial functions along the z direction. This set of trial functions is complete in the interval $(0, H)$, because the cosines form an orthogonal basis and have null derivatives, both at

$z = 0$ and $z = H$ and therefore the boundary conditions (7) and (8) do not hold generally. However, according to Strang & Fix (1973), pp. 11–13, the space of admissible functions includes trial functions such as eq. (16), which in the limit may give non-null derivatives at the edges of the domain. In fact, the weak form of the equation of motion (6) does not imply any requirement on the derivatives of the trial functions at the boundary. Note that the originally proposed set eq. (5) is composed of N orthogonal cosines and N orthogonal sines and the boundary conditions could be explicitly enforced.

The next step is to compute the integrals and solve the linear system of equations given by eq. (9) to obtain the unknown coefficients c_n in eq. (16).

2.1 Using the DCT and the DST to speed up calculations

Since the trial functions used in this scheme are cosine basis functions we are able to apply the discrete cosine transform (DCT) and the discrete sine transform (DST) to compute integrals (10), (12) and (13) in a faster way. Let N_{I} be the number of integration points along x or z. Using the discrete Fourier transform (DFT), the number of operations to compute the integrals is of the order of $O(N_{\mathrm{I}} \log N_{\mathrm{I}})$, whereas with the other strategy it is of the order of $O(N^2{}_{\mathrm{I}})$. Here we use the DCT-2, which uses $\cos[(j + \frac{1}{2})k\frac{\pi}{N}]$ (see Strang 1999). This corresponds to a mid-point rule cosine transform (second-order approximation rule). While it seems obvious that the power of the DFT ought to be applicable to computing numerical integration that involve sines and cosines (e.g. $\int_a^b \cos(\omega t)h(t)dt$), doing so turns out to be a surprisingly subtle matter. The problem lies in the oscillatory nature of the integrand. The consequence is that the result becomes systematically inaccurate as ω increases; see, e.g., Press *et al.* (1984) and Briggs & Henson (1995). However, in our case since we use a low order for the cosine basis functions ($N \leq N_{\mathrm{I}} \leq 128$) we do not need to worry about those inaccuracies. This is supported by the numerical comparisons shown in Section 4.

2.2 Choice of parameters

The solution is constructed with the trial functions $\psi^n(z) = \cos(\pi nz/H)$, where $n = 0, 1, \ldots, N - 1$. The wavelength associated with a function ψ^n is thus $\lambda_n = 2H/n$. To compute the solution for frequencies as high as $f_{\max}$ in a medium with velocities as low as $\beta_{\min}$, the number N of trial functions must be such that

$$\frac{2H}{N} \leq \lambda_{\min} \equiv \frac{\beta_{\min}}{f_{\max}}, \tag{17}$$

which implies that

$$\lambda_{\min} \geq 2\Delta z, \tag{18}$$

where H is the size of the model in one direction and N is the number of trial functions in this same direction, i.e. $H/N_{\mathrm{I}} = \Delta z$ along z.

Moreover, the number N_{I} of integration points, must be at least $N_{\mathrm{I}} \geq N$ in agreement with Shannon's principle (Shannon 1948). As we introduce discontinuities in the medium, the integration must be more accurate. Therefore, we must choose a larger value for N_{I}.

Let N and M be the number of trial functions along the z and x directions, respectively. Let $p = NM$ be the product of the number of trial functions along both directions, then the size of matrix (9) is $p \times p$. Thus in 2-D the size of the matrix to invert is p^2, and the cost of inversion of a full matrix is a p^3 process. Thus an estimate of the resolution times of our method grows (in 2-D) as the sixth power of p. This is indeed a serious limitation, and explains why we cannot practically use more than a few dozen trial functions. Eq. (18) gives the maximum frequencies we can compute: the minimum wavelength cannot be smaller than a few hundredth times the size of the model.

2.3 Comparisons between the Haskell method and the DSM for layered media

We show a 1-D numerical example to illustrate the feasibility and the accuracy of the DSM applied to a layered medium with cosines as basis functions. The example of an incident elastic plane wave on a layered system is well known; e.g. Ewing *et al.* (1957), Aki & Richards (1980). In particular, the propagator matrix formalism proposed by Thomson (1950) and later corrected by Haskell (1953) provides a systematic solution for the governing equations of elastodynamics. The use of the DFT displays no inaccuracies and computation is faster than when using traditional integration schemes.

In Fig. 2 synthetic seismograms from frequency domain results using the fast Fourier transform algorithm are displayed for 61 equally spaced receivers along z, the first receiver being that at the free surface. Fig. 2(a) corresponds to results obtained using the DSM and Fig. 2(b) corresponds to the Haskell results for the same scale. A layered model contains three layers with the following properties: $\beta_1 = 700\,\mathrm{m\,s^{-1}}$, $\rho_1 = 1750\,\mathrm{kg\,m^{-3}}$, $\beta_2 = 800\,\mathrm{m\,s^{-1}}$, $\rho_2 = 2000\,\mathrm{kg\,m^{-3}}$, $\beta_3 = 1200\,\mathrm{m\,s^{-1}}$, $\rho_3 = 3000\,\mathrm{kg\,m^{-3}}$ and $\beta = 2000\,\mathrm{m\,s^{-1}}$, $\rho = 5000\,\mathrm{kg\,m^{-3}}$. The layers are 300, 300 and 400 m thick, respectively. The number of trial functions used in this experiment is $N = 64$. Fig. 2(c) displays both solutions plotted together for station no 1. Fig. 2(d) shows the excellent agreement between these two methods. Here the percentage error at station no 1 located at (0, 0) is less than 1.2 per cent. The error is computed as

$$\mathrm{error}(t) = (|a(t) - n(t)|/|a(t)|) \times 100, \tag{19}$$

where $a(t)$ is the analytic displacement at time t and similarly $n(t)$ is the numerical displacement at time t computed with the DSM. No reflection is seen in the lower boundary, as the absorbing boundary conditions used are exact (we have perfect plane waves with known wavenumbers in this case).

3 THE DIRECT SOLUTION METHOD FOR THE 2-D CASE

We now consider a 2-D lattice to represent the inhomogeneous medium. The elastic parameters will now be functions dependent on x and z. As in the 1-D case the strong form for the elastic equation of motion in the spectral domain (ω, x, z) could be defined. We will only give details for the weak form operator. The incident field is given by eq. (2) and v is as in eq. (1) but now with a dependence on the spatial variables x and z. We write the driving field for this case as $v^{(0)}(x,z) = \mathrm{e}^{-ik_x x + ik_z z}$. The displacement function $V(x, z)$ is of the form

$$V(x, z) = \sum_{n=0}^{N-1} \sum_{m=0}^{M-1} c_{nm} \psi^n(z) \varphi^m(x), \tag{20}$$

where

$$\psi^n(z) = \cos\left(\frac{n\pi z}{H}\right) \quad \text{and} \quad \varphi^m(x) = \cos\left(\frac{m\pi x}{L}\right), \tag{21}$$

with H and L being the dimensions of the model along z and x, respectively. The number of trial functions along z and x is N and M, respectively, and the expansion coefficients c_{nm} are the unknowns. The displacement $v(x, z)$ is similar to eq. (1), but replacing function

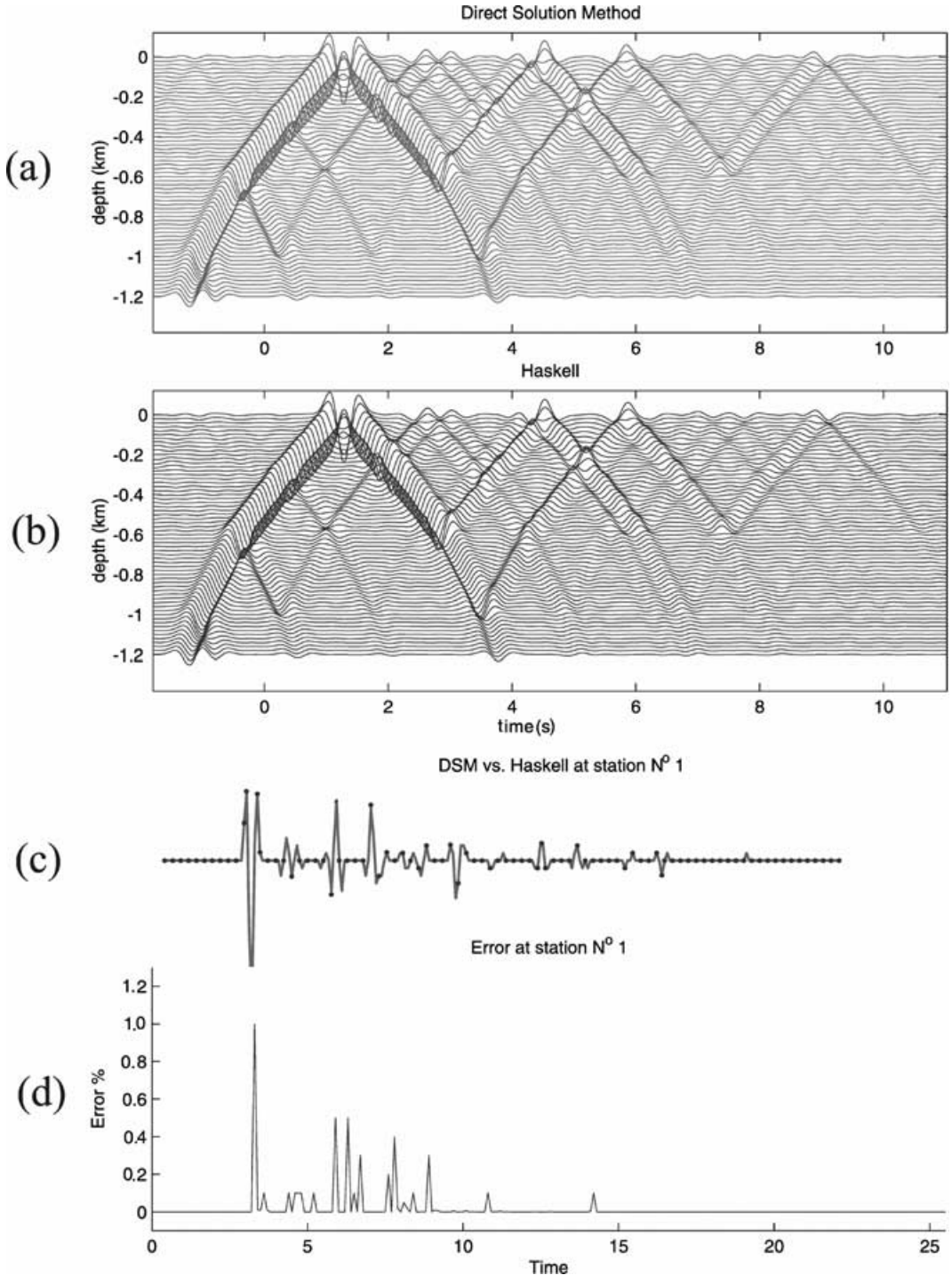

Figure 2. Synthetic seismograms showing the results of displacements obtained using (a) the DSM and (b) the Haskell method for three layers with the following properties: $\beta_1 = 700$ m s^{-1}, $\rho_1 = 1750$ kg m^{-3}, $\beta_2 = 800$ m s^{-1}, $\rho_2 = 2000$ kg m^{-3}, $\beta_3 = 1200$ m s^{-1}, $\rho_3 = 3000$ kg m^{-3} and $\beta = 2000$ m s^{-1}, $\rho = 5000$ kg m^{-3}. The layers have thickness of 300, 300 and 400 m, respectively. A set of 61 equally spaced receivers are located along the z-axis, the first receiver being that at the free surface. The number of trial functions used in this experiment is $N = 64$. We can see the reflections in various layers, and the amplification at the free surface. No reflection is seen in the lower boundary, as the absorbing boundary conditions used are exact (we have perfect plane waves with known wavenumbers in this case). (c) Both solutions are plotted together for station no 1. (d) Of particular significance is the excellent agreement between these two methods. Here the percentage error at station no 1 located at (0, 0) is less than 1.2 per cent.

$V(x, z)$ by eq. (20) and using the corresponding driving field $v^{(0)}(x, z)$. For simplicity in the computation, as in the 1-D case, we are using only cosines as basis functions. Let us define the following auxiliary functions:

$$\mathcal{R}(n, m) = \int_0^L \left[\psi^n(H)\mu v_{,z}(x, H) - \psi^n(0)\mu v_{,z}(x, 0)\right]\varphi^m(x)\, dx \tag{22}$$

and

$$\mathcal{P}(m, n) = \int_0^H \left[\varphi^m(L)\mu v_{,x}(L, z) - \varphi^m(0)\mu v_{,x}(0, z)\right]\psi^n(z)\, dz, \tag{23}$$

where the subscripts '$,x$' and '$,z$' denote differentiation with respect to x and z, respectively. Using eqs (22) and (23), the weak form operator (analogous to eq. 6) for the 2-D case is given by

$$\int_0^L \int_0^H [\psi^n\varphi^m\rho\omega^2 v - \psi^n_{,z}\varphi^m\mu v_{,z} - \psi^n\varphi^m_{,x}\mu v_{,x}]\, dz\, dx \tag{24}$$

$$+\mathcal{R}(n, m) + \mathcal{P}(m, n) = 0 \quad (n = 0, \ldots, N-1;\ m = 0, \ldots, M-1). \tag{25}$$

As in the 1-D case integrating by parts (24), the strong form can be obtained. The boundary conditions included in the weak form operator are:

$$\mu\left(\frac{\partial V}{\partial x}\right)^n = i\mu V^n(0, z) \quad x = 0, \text{ left boundary}, \tag{26}$$

$$\mu\left(\frac{\partial V}{\partial x}\right)^n = -i\mu V^n(L, z) \quad x = L, \text{ right boundary}, \tag{27}$$

$$\mu\left(\frac{\partial V}{\partial z}\right)^m = i\mu V^m(x, 0) \quad z = 0, \text{ upper boundary}, \tag{28}$$

$$\mu\left(\frac{\partial V}{\partial z}\right)^m = -i\mu V^m(x, H) \quad z = H, \text{ lower boundary}, \tag{29}$$

where V^n and V^m are given by

$$V^n(x, z) = \sum_{m=0}^{M-1} c_{nm}\psi^n(z)\varphi^m(x)k_x^n \tag{30}$$

and

$$V^m(x, z) = \sum_{n=0}^{N-1} c_{nm}\psi^n(z)\varphi^m(x)k_z^m \tag{31}$$

with k_x^n and k_z^m defined as

$$k_x^n = \sqrt{\frac{\omega^2}{\beta^2} - \frac{n^2\pi^2}{H^2}} \tag{32}$$

and

$$k_z^m = \sqrt{\frac{\omega^2}{\beta^2} - \frac{m^2\pi^2}{L^2}} \tag{33}$$

are the local wavenumbers. With an appropriate condition on the sign of its imaginary part, so it corresponds to a wave that is not growing in amplitude outside the domain of interest. Note that these conditions are local, i.e. they are valid at the boundary for each term of the cosines expansion, precisely as a consequence of using these functions. The idea for these boundary conditions is to express, through the normal derivative of the displacement (i.e. traction) at a given boundary point, the outgoing radiation condition in terms of a linear combination of boundary values. This concept links both Dirichlet and Neumann boundary conditions. Thus the mathematical device to describe this is called the Dirichlet-to-Neumann operator (DtN), which is a term coined in the mathematical community (Givoli & Keller 1990; Givoli 1991).

These absorbing boundary conditions at the outer boundary ($z = 0, z = H, x = 0$ and $x = L$) are implicitly included in the weak form operator (24) and will then be naturally satisfied. These conditions are verified exactly for a plane wave and a plane boundary. It turns out that for the cosine basis that we are using, the same is true and this is of more general validity, as shown in the Appendix.

In order to write the matrix form expressions for eq. (24) we define the following auxiliary functions:

$$\hat{R}(n, s, m, r) = \int_0^L \left[\psi^n(H)\mu\psi^s_{,z}(H) - \psi^n(0)\mu\psi^s_{,z}(0)\right]\varphi^m(x)\varphi^r(x)\, dx, \tag{34}$$

and

$$\hat{R}^0(n, m) = \int_0^L \left[\psi^n(H)\mu v^{(0)}_{,z}(x, H) - \psi^n(0)\mu v^{(0)}_{,z}(x, 0)\right]\varphi^m(x)\, dx, \tag{35}$$

for integration along x. Similarly for the variable z we have

$$\hat{P}(m, r, n, s) = \int_0^H \left[\varphi^m(L)\mu\varphi^r_{,x}(L) - \varphi^m(0)\mu\varphi^r_{,x}(0)\right]\psi^n(z)\psi^s(z)\, dz, \tag{36}$$

and

$$\hat{P}^0(m, n) = \int_0^H \left[\varphi^m(L)\mu v^{(0)}_{,x}(L, z) - \varphi^m(0)\mu v^{(0)}_{,x}(0, z)\right]\psi^n(z)\, dz. \tag{37}$$

Hence, in matrix form eq. (24) can be written as in eq. (9) where the explicit matrices and vector for the 2-D case are given by

$$T_{mn,rs} = \int_0^H \int_0^L \psi^n\varphi^m\rho\psi^s\varphi^r\, dx\, dz,$$

$$T^0_{mn} = \int_0^H \int_0^L \psi^n\varphi^m\rho v^{(0)}\, dx\, dz, \tag{38}$$

$$H_{mn,rs} = \int_0^H \int_0^L \left[\psi^n_{,z}\varphi^m\mu\psi^s_{,z}\varphi^r + \psi^n\varphi^m_{,x}\mu\psi^s\varphi^r_{,x}\right] dx\, dz, \tag{39}$$

$$H^0_{mn} = \int_0^H \int_0^L \left[\psi^n_{,z}\varphi^m\mu v^{(0)}_{,z} + \psi^n\varphi^m_{,x}\mu v^{(0)}_{,x}\right] dx\, dz, \tag{40}$$

$$R_{mn,rs} = \hat{R}(n, s, m, r) + \hat{P}(m, r, n, s), \tag{41}$$

$$R^0_{mn} = \hat{R}^0(n, m) + \hat{P}^0(m, n). \tag{42}$$

Let $p = NM$ be the product of the number of both trial functions (along z and x). Note that in eqs (38), (39) and (41) we have two double indices, which correspond to $p \times p$ matrices.

The efficient computation of the coefficients of the **T** and **H** matrices requires the use of mixed cosine/sine transforms in the x and z directions.

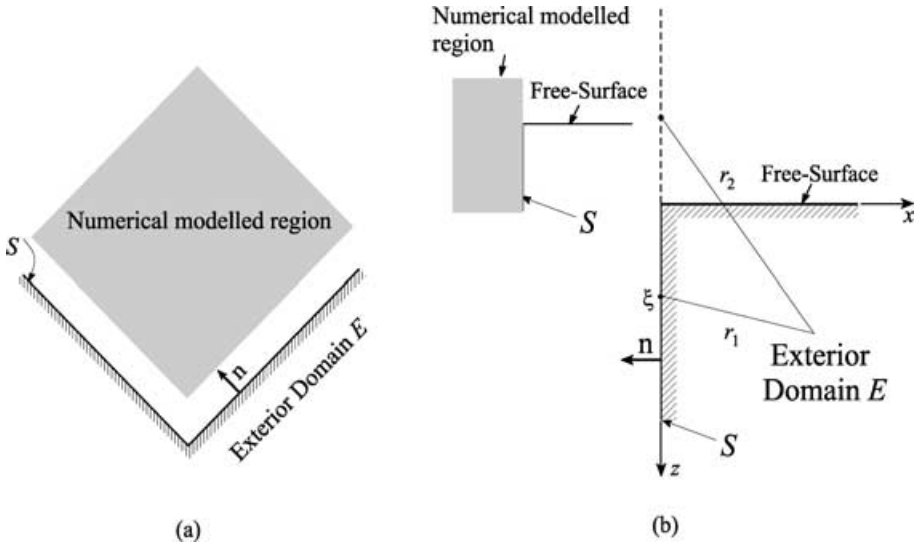

Figure 3. The stiffness approach is used to impose free-surface and absorbing boundary conditions. The vector **n** normal to the boundary S and the region under scrutiny depend on the case under study. (a) Stiffness for a three-quarter-space corresponds to the absorbing boundary condition for one corner of the domain. (b) Stiffness for a quarter-space corresponds to the free surface. In this case $r_1 = \sqrt{(z-\xi)^2 + x^2}$ and $r_2 = \sqrt{(z+\xi)^2 + x^2}$ and the Green's function is given by $G(\mathbf{x}, \mathbf{x}_0, \omega) = \frac{1}{4i\mu}\{H_0^{(2)}(kr_1) + H_0^{(2)}(kr_2)\}$.

3.1 Computation of the stiffness

Inspired by Kausel & Roesset (1981) and their interpretation of half-space stiffness as being equivalent to a perfect absorber, we develop a method to correct spurious reflections created at the corners of the computational domain. The idea is to relate in a discrete sense the tractions and displacements at the surface of a domain (which is exterior to the numerical grid) with the stiffness matrix. When we calculate the tractions given by the integral in eq. (A9), we approximate this value since the computation is with discrete values. Therefore, there is an error produced by the discretization. To reduce this error we compute the stiffness matrix of the exterior region using the indirect boundary element method (IBEM). For further details on the IBEM see Sánchez-Sesma & Campillo (1991).

In order to compute the stiffness using the IBEM consider a corner of the discretized model, with homogeneous elastic properties. The associated integral equations are given by

$$v(\mathbf{x}) = \int_S G(\mathbf{x}, \xi)\phi(\xi)\, dS_\xi \tag{43}$$

and

$$t(\mathbf{x}) = \frac{1}{2}\phi(\mathbf{x}) + \int_S T(\mathbf{x}, \xi)\phi(\xi)\, dS_\xi, \tag{44}$$

where v is the displacement on the boundary S, $G(\mathbf{x}, \xi)$ is Green's function given by

$$G(\mathbf{x}, \mathbf{x}_0) = \frac{1}{4i\mu} H_0^{(2)}\left(\frac{\omega r}{\beta}\right) \tag{45}$$

with $r = |\mathbf{x} - \mathbf{x}_0|$, $\mathbf{x}$ the observer and $\mathbf{x}_0$ denotes the source point. $H_0^{(2)}(\cdot)$ is the Hankel function of the second kind and order 0. The traction at the boundary is given by t, $T(\mathbf{x}, \xi)$ is the traction Green's function, which is normally oriented outward (relative to the exterior domain, see Fig. 3a) and ϕ is the force density. It follows that

$$\mathbf{t} = \left(\frac{1}{2}\mathbf{I} + \mathbf{T}\right)\mathbf{G}^{-1}\mathbf{v}. \tag{46}$$

We then obtain, the stiffness matrix $\mathbf{K}$:

$$\mathbf{K} = \left(\frac{1}{2}\mathbf{I} + \mathbf{T}\right)\mathbf{G}^{-1}. \tag{47}$$

The same approach can be applied to impose the free-surface boundary conditions that correspond to a half-space. We follow the same analysis but instead of keeping in view a three-quarter-space we consider only a quarter-space (see Fig. 3b). We start from the same equations, but divide the interfaces into three domains (as indicated in Fig. 3b). As in eq. (43) we write for $\mathbf{x}$ on E, the exterior domain:

$$v(\mathbf{x}) = \int_S G(\mathbf{x}, \xi)\phi(\xi)\, dS_\xi \tag{48}$$

now with S running along the positive values of z at $x = 0$ and the Green's function given by

$$G(\mathbf{x}, \mathbf{x}_0, \omega) = \frac{1}{4i\mu}\left\{H_0^{(2)}(kr_1) + H_0^{(2)}(kr_2)\right\}, \tag{49}$$

where $r_1 = \sqrt{(z-\xi)^2 + x^2}$ and $r_2 = \sqrt{(z+\xi)^2 + x^2}$. In this way the surface $x > 0$, $z = 0$ is traction-free. We construct Green's function using the images method. Along the boundary S ($x = 0$, $z > 0$) the tractions are given by eq. (44), but

$$T = \mu\frac{\partial G}{\partial n}\bigg|_{x=0} = -\mu\frac{\partial G}{\partial z}\bigg|_{x=0} = 0 \tag{50}$$

and then from eqs (48) and (44) we can write

$$\mathbf{t} = \frac{1}{2}\mathbf{G}^{-1}\mathbf{v} \tag{51}$$

and the stiffness matrix is simply

$$\mathbf{K} = \frac{1}{2}\mathbf{G}^{-1}. \tag{52}$$

We use the stiffness matrix approach for a quarter-space to impose free-surface boundary conditions. The model consists of a

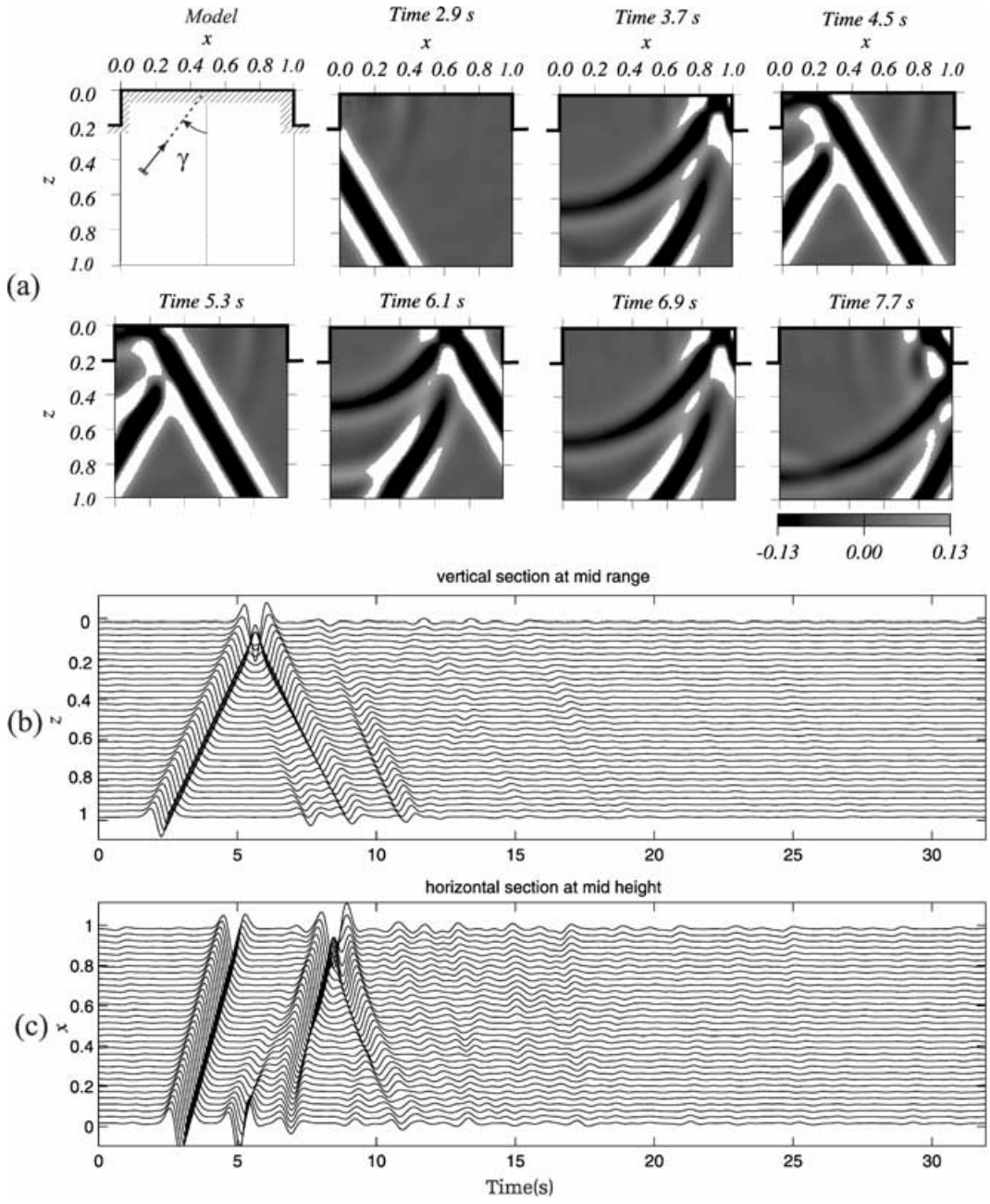

Figure 4. We use the stiffness matrix approach for a quarter-space to impose free-surface boundary conditions. The model consists of a rectangular prominence over a half-space of 0.2 m in height subjected to an incident plane wave with an incident angle $\gamma = 30^\circ$. (a) Snapshots for a square grid of 128 × 128 equally spaced receivers. The time variation of the incoming wavefield is a Ricker wavelet with a characteristic period $t_p = 1/\beta$ s. We have used 32 × 32 trial cosine functions, 128 × 128 integration points and $L = H = 1$ m. (b) Synthetic seismograms for 32 equally spaced receivers located along the z-axis. Note that the amplitude of the *SH* waveform at the free surface is exactly twice that of incident and reflected waves. This illustrates the accuracy of the free-surface boundary condition. (c) Synthetic seismograms for 32 equally spaced receivers located along the x-axis.

rectangular prominence over a half-space of 0.2 m in height subjected to an incident plane wave with an incident angle $\gamma = 30^\circ$. In Fig. 4(a) a set of snapshots is computed from the frequency-domain results using the FFT. We have a mesh of 128 × 128 equally spaced receivers. In Fig. 4(b) we have synthetic seismograms for 32 equally spaced receivers along the line $z = 0.5$. Similarly in Fig. 4(c) we have synthetic seismograms for receivers along the line $x = 0.5$. We can see reflections produced at the free surface and reflections and diffraction at the corners of the prominence.

3.1.1 Advantages and disadvantages of the use of the stiffness matrix

We reduced spurious reflections produced at the corners using the stiffness matrix for a three-quarter-space. Computing the stiffness matrix for a quarter-space enables us to impose free-surface boundary conditions. One approach to test the efficiency of the stiffness matrix is that of Fig. 5. A line source is applied at the centre of (i.e. (0, 0)) a homogeneous medium with $\beta = 1$ m s^{-1} and $\rho = 1$ kg m^{-3}. The results obtained with the DSM plus the stiffness matrix and only

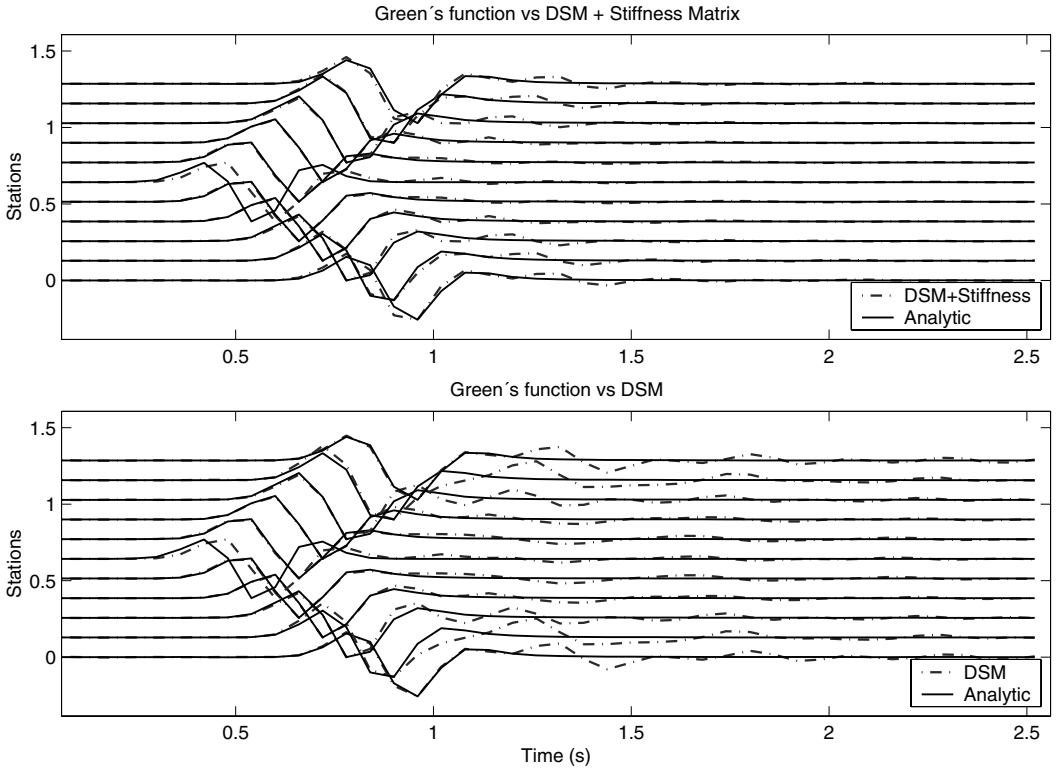

Figure 5. The use of the stiffness approach enhances the absorbing boundaries. A line source is applied at the centre of (i.e. (0, 0)) a homogeneous medium with $\beta = 1$ m s^{-1} and $\rho = 1$ kg m^{-3}. The results obtained with the DSM plus the stiffness matrix and with the DSM are compared with those generated with the analytical solution $G(\mathbf{x}, \mathbf{x}_0, \omega) = (1/4i\mu)\ H_0^{(2)}(\omega\, r/\beta)$, where $r = |\ \mathbf{x} - \mathbf{x}_0|$. A set of 11 equally spaced receivers is located along the line $z = x$. The time variation of the incoming wavefield is a Ricker wavelet with characteristic period $t_p = 1/2\beta$s, with $L = H = 1$ m. When using the absorbing boundary conditions (26)–(29) the oscillations are very strong. When appropriately adding the stiffness matrix the oscillations are reduced especially for stations located close to the corners.

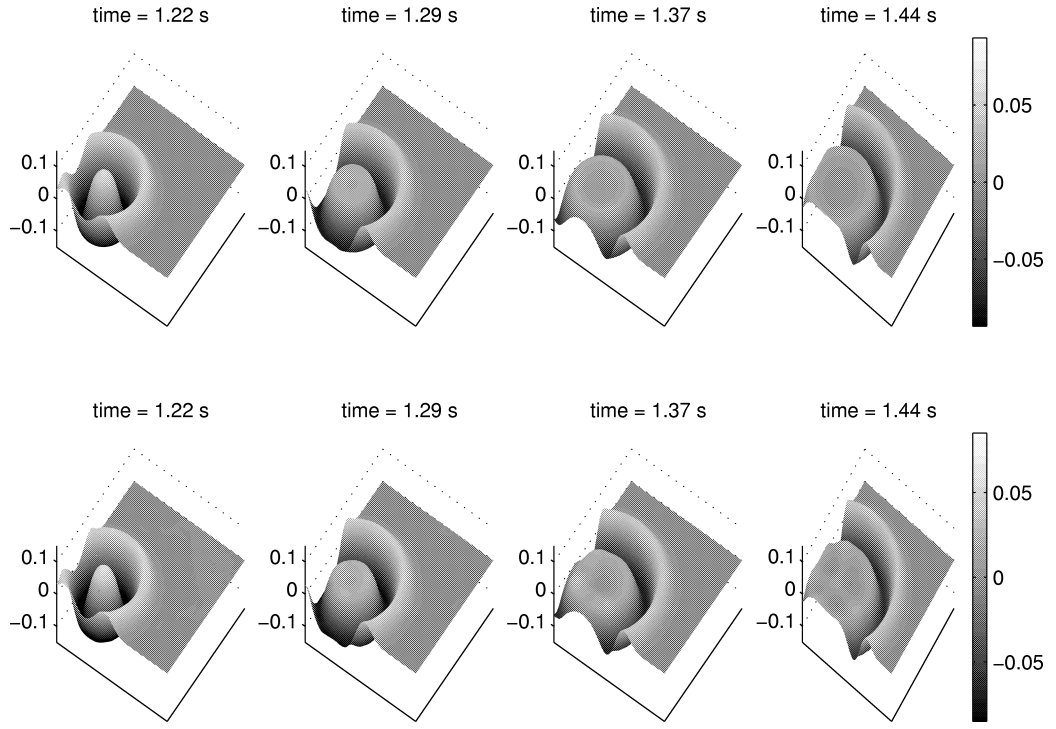

Figure 6. Top, the analytical solution given by Green's function $G(\mathbf{x}, \mathbf{x}_0, \omega) = (1/4i\mu)\ H_0^{(2)}(\omega r/\beta)$, where $r = |\ \mathbf{x} - \mathbf{x}_0|$. Bottom, snapshots for the corresponding solution obtained using the DSM. A line source is being applied at the point (0.25 m, 0.25 m) within a homogeneous medium (with $\beta = 1$ m s^{-1} and $\rho = 1$ kg m^{-3}), the origin is at the lower left-hand corner. A mesh of 101 × 101 equally spaced receivers is located within a 1 m square. Even though there are some spurious reflections, the results show a fair agreement with the analytic solution.

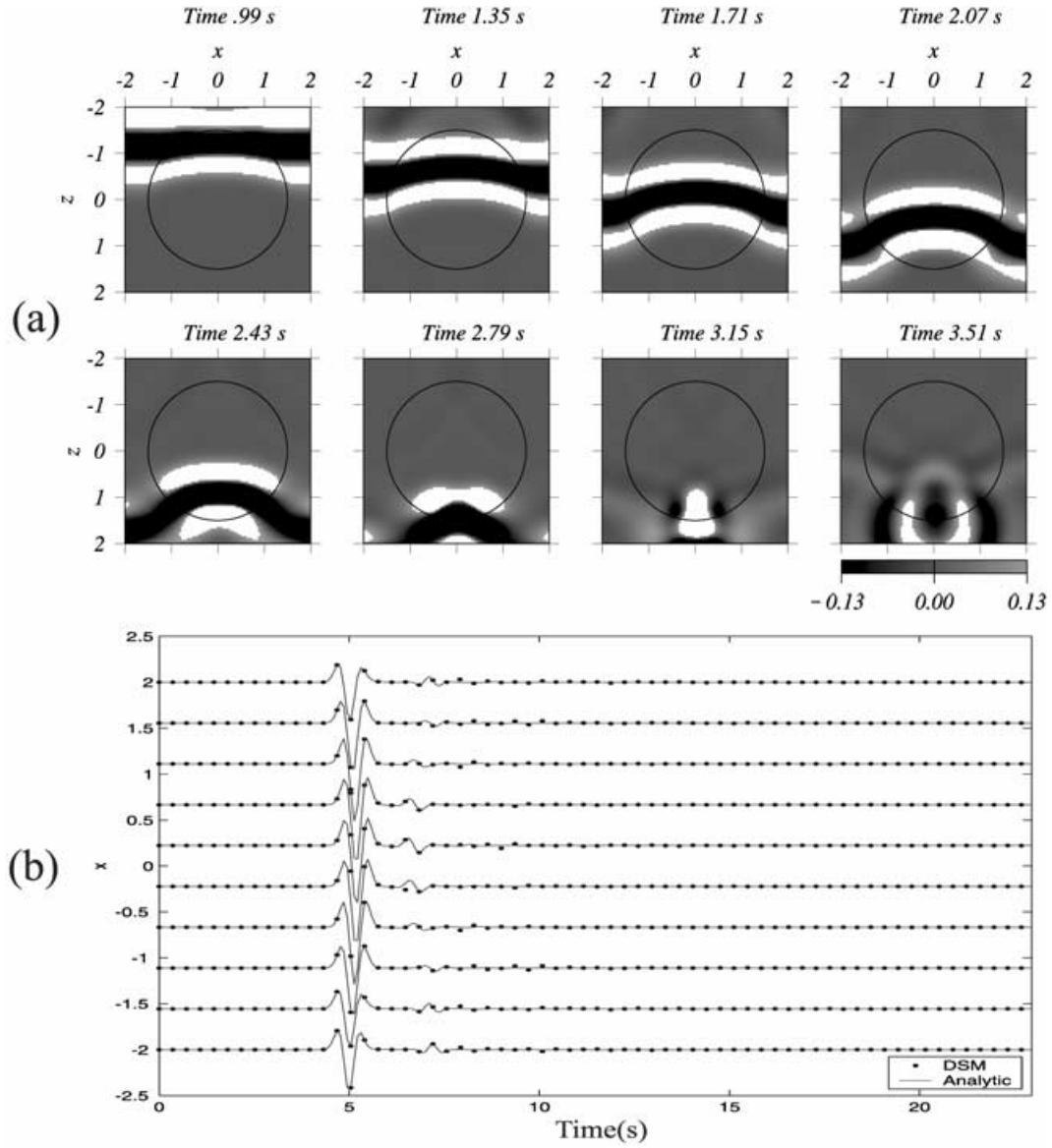

Figure 7. (a) Results obtained using the DSM for one cylinder within a square of size $H = L = 4$ m. The elastic parameters for the surrounding medium are $\beta = 2$ m s^{-1}, $\rho = 2$ kg m^{-3}, and for the cylinder $\beta_R = 1.5$ m s^{-1}, $\rho_R = \rho$ radius $r = 1.5$ m. We used 52×52 cosine trial functions and 128×128 integration points. Snapshots for a mesh of 101×101 equally spaced receivers. The incident time signal is a Ricker wavelet with characteristic period $t_p = 0.75$ s. We note a good agreement between the analytical and the numerical solution. (b) Comparison between the analytical solution and the DSM solution for a line of receivers located along $y = 0$ and $x \in [-2, 2]$. The stations close to $x = 0$ have a delay due to the fact that the velocity inside the cylinder is less than in the surrounding medium.

with the DSM are compared with those generated with the analytical solution given by eq. (45). A set of 11 equally spaced receivers is located along the line $z = x$. The time variation of the incoming wavefield is a Ricker wavelet with the characteristic period $t_p = 1/2\beta$ s, where $L = H = 1$ m. In another approach one uses the absorbing boundary conditions (26)–(29). The oscillations are very strong, whereas, when appropriately adding the stiffness matrix, the oscillations are drastically reduced. The correction is noticeable in particular for receivers located close to the corners where there are considerable differences in oscillations. When computing the integrals in eqs (41) and (42), i.e. when we apply the absorbing boundary conditions, we are assuming that the values of the tractions (defined as t_y^0) along the boundary are well approximated. However, we can see some undesirable oscillations in Fig. 5. In order to compute integrals in eqs (41) and (42) it is necessary to integrate by parts. In this process we note that a product of two pairs of trial functions (say $\varphi^m \psi^n$ and $\varphi^r \psi^s$) contributes to these integrals. By examining the value of this product at the corners we conclude that the factor

$$c = 1 + (-1)^{s+n} + (-1)^{m+r} + (-1)^{m+n+r+s} \tag{53}$$

is the input of each corner to the tractions (t_y^0) computed in eqs (26)–(29). When replacing the expressions in eqs (41) and (42), that involve this particular product with $t_y - ct_y^0$ (where t_y are the tractions computed with the IBEM) we obtain an appropriate correction for each corner. This reduces the spurious reflections.

Nevertheless, it is important to point out that the stiffness matrix is frequency dependent. Since we only need to compute a few values

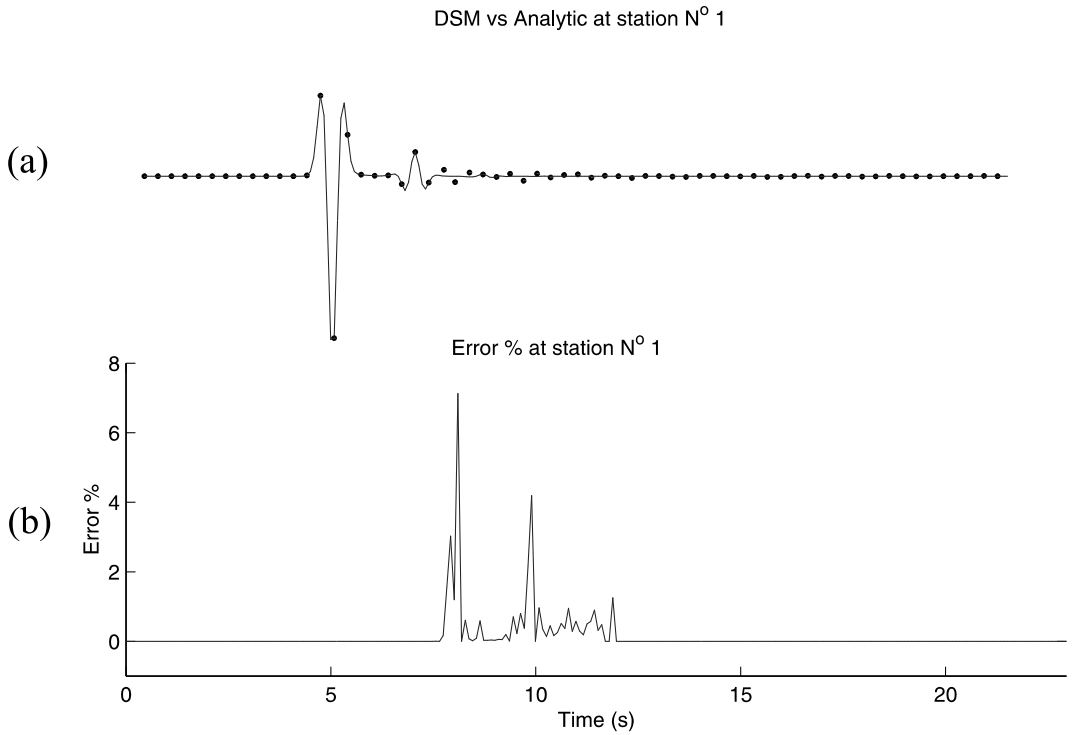

Figure 8. (a) The solution obtained with the DSM for the elastic cylinder in Fig. 7 is plotted with the analytical solution for station no 1. In order to measure the error we have plotted (b) the percentage error at station no 1 located at $(-2, 0)$ where we can see that the biggest difference is less than 8 per cent. Station no 1 was chosen because the biggest differences are shown at receivers located close to $x = \pm 2$.

near the corners we believe it is possible to find a strategy to compute it only once and use the result as an approximation for all the needed frequencies. However, this is a subject of further work.

4 NUMERICAL RESULTS

We test the method with two simple problems for which analytical solutions are known. The first problem consists of a homogeneous medium with an impulsive line source. The analytical solution for this problem is given by the Green's function (45). Fig. 6 at the top, displays the analytical solution given by eq. (45) for a line source applied at (0.25 m, 0.25 m). The results obtained using the DSM are shown at the bottom in Fig. 6. We compute snapshots for a mesh with 101×101 equally spaced receivers located within a 1 m long square. The results are encouraging since both solutions are similar and the absorbing boundaries are acting as expected. The second problem concerns a cylindrical inclusion within a homogeneous medium the size of which is $H = L = 4$ m. This is a classic solution based on a Bessel series expansion (the reader is referred to Mow & Pao 1971). In Fig. 7(a) we have results obtained using the DSM for one cylinder within a square of size $H = L = 4$ m. The elastic parameters for the surrounding medium are $\beta = 2$ m s^{-1}, $\rho = 2$ kg m^{-3}, and for the cylinder $\beta_R = 1.5$ m s^{-1}, $\rho_R = \rho$, ratio $r = 1.5$ m. We compute snapshots for a mesh with 101×101 equally spaced receivers, using 52×52 cosine trial functions and 128×128 integration points. The incident time signal is a Ricker wavelet with characteristic period $t_p = 0.75$ s.

In Fig. 7(b) a comparison between the analytical solution and the DSM solution for a line of receivers located along $y = 0$ and $x \in [-2, 2]$ is shown. The stations close to $x = 0$ have a delay due to the fact that the velocity inside the cylinder is less than in the surrounding medium. We see small differences, although these are greater at receivers located close to $x = \pm 2$. In order to measure the error we have plotted the percentage error at station no 1 (the corresponding synthetic seismogram is in Fig. 8a) located at $(-2, 0)$ we can see in Fig. 8(b) that the biggest difference is less than 8 per cent. The percentage error at each time t in the synthetics was computed as in eq. (19). In this example the diffraction is noticeable when the wave reaches the cylinder and the wave front is curved due to the presence of the inclusion with smaller velocity. Note that the agreement between the analytical and numerical solutions is good and the error in the worst cases is less than 8 per cent. Therefore, the method reproduces the physical phenomena accurately.

The next experiment is a set of vugs or inclusions with the same elastic properties different from the surrounding medium and different sizes. In Fig. 9 we have four elastic cylinders within a square medium of size $H = L = 4$ m. The elastic parameters are $\beta = 1$ m s^{-1}, $\rho = 1$ kg m^{-3} (the surrounding medium), for the cylinders $\beta_1 = \beta_2 = \beta_3 = \beta_4 = 0.8$ m s^{-1}, $\rho_1 = \rho_2 = \rho_3 = \rho_4 = \rho$, ratios $r_1 = 0.4$ m, $r_2 = 0.52$ m, $r_3 = 0.8$ m and $r_4 = 0.72$ m. We used 55×55 cosine trial functions and 128×128 integration points. Note that the cylinders at the top act as a barrier that attenuates the wave that reaches the second row of heterogeneities. Part of the energy trapped inside each cylinder comes out and produces diffraction, the rest produces diffraction that bounces backwards and forwards until the energy is lost. As time increases the wave front recovers and the scattering effect caused by the inclusions on the plane wave diminishes.

Note that if we have an infinite and complete basis then we obtain (in this limit) the correct solution, even if all of the trial functions are such that the natural boundary condition of continuity of

Figure 9. Snapshots for a mesh of 101 × 101 equally spaced receivers. Four cylinders within a square medium of size $H = L = 4$ m. The elastic parameters are β= m s^{-1}, $\rho = 1$ kg m^{-3} (the surrounding medium), for the cylinders $\beta_1 = \beta_2 = \beta_3 = \beta_4 = 0.8$ m s^{-1}, $\rho_1 = \rho_2 = \rho_3 = \rho_4 = \rho$, ratios $r_1 = 0.4$ m, $r_2 = 0.52$ m, $r_3 = 0.8$ m and $r_4 = 0.72$ m. We used 55 × 55 cosine trial functions and 128 × 128 integration points. The wave front attenuates while traversing the cylinders as do the interactions between the scattered waves.

traction cannot be rigorously satisfied at the lithological boundaries. On the other hand, we obviously always have a finite basis in any real computation. The numerical solutions of the present approach will therefore always be subject to error due to the failure to satisfy continuity of traction at the boundaries of the cylinders and the surrounding media. This is a problem of all discrete numerical techniques. However, for a desired resolution one can increase the number of trial functions and this will obviously increase the computational cost. For the example given in Fig. 9 medium parameters are not realistic, this is again a problem of costs. Provided a large

number of trial functions we could still have good agreement for realistic cases.

Numerical examples given in Figs 4, 7 and 9 were the most expensive computations, generated on a Pentium 4, 1.7 MHZ taking 40 h of CPU time.

5 CONCLUSIONS

We have shown the feasibility of simulate wave propagation in heterogeneous media using the DSM. Applying the stiffness matrix for a three-quarter-space we are able to reduce spurious reflections generated at the corners. This strategy improves the solution compared with that obtained using regular absorbing boundaries given by eqs (26)–(29). When computing the stiffness matrix for a quarter-space we have managed to impose free-surface boundary conditions. It should be pointed out that, since the stiffness matrix is frequency dependent, computational costs could be high. We also note that either by increasing the number of trial functions or by using the stiffness matrix we obtain an improved solution. However, both approaches are expensive. Reducing these costs is a subject of further scrutiny.

A current limitation of this method is the fact that the minimum wavelength used has to be at least twice the size of the model divided by the number of trial functions. This limits the resolution because the size and number of heterogeneities together with its elastic properties are constrained by the number of trial functions used. If more trial functions are needed the resulting systems of linear equations become very large. Parallel computing for methods in the frequency domain is much simpler than time domain computation based on domain decomposition. This is an advantage of the DSM and it will help to reduce this problem. The use of cosine basis functions allows us to use the fast Fourier transform to compute more efficiently the integrals needed to fill the matrix corresponding to the linear system to be solved. This helps alleviate the computational burden. However, we should point out that the number of trial functions p is increasing strongly with the number of heterogeneities. The computation time is proportional to p^3. Therefore, for a really complex medium containing small-scale heterogeneities (for example, a random medium), the computational time would be huge (even using the DCT/DST). Thus the method would not be appropriate for modelling 2-D multiscale complex media, in comparison with standard finite-difference techniques.

Numerical results from the application of the stiffness concept are encouraging and, even though there are still some spurious reflections generated at the corners, the improvement is significant. The physical phenomena are well reproduced in all the tested cases.

ACKNOWLEDGMENTS

We thank T. Bohlen, T. Furumura, D. Komatitsch, R. Vai and L. F. Larson for valuable comments that helped to improve the manuscript. We specially thank N. Takeuchi and R. Geller for fruitful discussions on the DSM. We also thank R. Avila-Carrera for kindly providing us with a version of a program for the 1-D case which was a guide for the further developments. This work has been partially supported by Instituto Mexicano del Petróleo under project D.00117, by DGAPA-UNAM, México under grant IN121202 and by Conacyt México under project NC-204.

REFERENCES

Abramowitz, M. & Stegun, I.A. (eds.), 1970. *Handbook of Mathematical Functions,* Dover, New York.

Aki, K. & Richards, P.G., 1980. *Quantitative Seismology,* Freeman, San Francisco.

Bérenger, J.P., 1994. A perfectly matched layer for the absorption of electromagnetic waves, *J. Comput. Phys.,* **114,** 185–200.

Briggs, W. & Henson, V., 1995. *The DFT: an Owner's Manual for the Discrete Fourier Transform,* SIAM, Philadelphia.

Clayton, R. & Engquist, B., 1977. Absorbing boundary conditions for acoustic and elastic wave equations, *Bull. seism. Soc. Am.,* **67,** 1529–1540.

Collino, F. & Tsogka, C., 2001. Application of the perfectly matched absorbing layer model to the linear elastodynamic problem in anisotropic heterogeneous media, *Geophysics,* **66,** 294–307.

Cummins, P., 1994. DSM complete synthetic seismograms: SH, spherically symmetric case, *Geophys. Res. Lett.,* **21,** 533–566.

Cummins, P., Takeuchi, N. & Geller., R., 1997. Computation of complete synthetic seismograms for laterally heterogeneous models using the direct solution method, *Geophys. J. Int.,* **130,** 1–16.

Ewing, M., Jardetzky, W. & Press, F., 1957. *Elastic Waves in Layered Media,* McGraw-Hill, New York.

Frankel, A. & Clayton, R.W., 1986. Finite differences simulations of seismic scattering: implications for the propagation of short-period seismic waves in the crust and models of crustal heterogeneity, *J. geophys. Res.,* **91,** 6465–6489.

Geller, R. & Ohminato, T., 1994. Computation of synthetic seismograms and their partial derivatives for heterogeneous media with arbitrary natural boundary conditions using the direct solution method, *Geophys. J. Int.,* **116,** 421–446.

Geller, R. & Takeuchi, N., 1995. A new method for computing highly accurate DSM synthetic seismograms, *Geophys. J. Int.,* **123,** 449–470.

Givoli, D., 1991. Non-reflecting boundary conditions: review article, *J. Comput. Phys.,* **94,** 1–29.

Givoli, D. & Keller, J.B., 1990. Non-reflecting boundary conditions for elastic waves, *Wave motion,* **12,** 261–279.

Hara, T., Tsuboi, S. & Geller, R., 1993. Inversion for laterally heterogeneous upper mantle *S*-wave velocity structure using iterative waveform inversion, *Geophys. J. Int.,* **115,** 667–698.

Haskell, N.A., 1953. The dispersion of surface waves on multilayered media, *Bull. seism. Soc. Am.,* **43,** 17–34.

Higdon, R.L., 1990. Radiation boundary conditions for elastic wave propagation, *SIAM J. Numer. Anal.,* **27,** 831–870.

Kausel, E., 1992. Physical interpretation and stability of paraxial boundary conditions, *Bull. seism. Soc. Am.,* **82,** 898–913.

Kausel, E. & Roesset, J., 1981. Stiffness matrices for layered solids, *Bull. seism. Soc. Am.,* **71,** 1743–1761.

Kosloff, R. & Kosloff, R., 1986. Absorbing boundaries for wave propagation problems, *J. Comput. Phys.,* **63,** 363–376.

Mow, C.C. & Pao, Y.H., 1971. The diffraction of elastic waves and dynamic stress concentrations, *United States Air Force Project Rand,* Report R-482-PR.

Peng, C. & Toksöz, M., 1994. An optimal absorbing boundary condition for finite difference modeling of acoustic and elastic wave propagation, *J. acoust. Soc. Am.,* **95,** 733–745.

Peng, C. & Toksöz, M., 1995. An optimal absorbing boundary condition for elastic wave modeling, *Geophysics,* **60,** 296–301.

Press, W., Teukolosky, S., Vetterling, W. & Flannery, B., 1984. *Numerical Recipes in Fortran 77: the Art of Scientific Computing,* Cambridge University Press, Cambridge.

Sánchez-Sesma, F.J. & Campillo, M., 1991. Diffraction of *P*, *SV* and Rayleigh waves by topographic features, *Bull. seism. Soc. Am.,* **81,** 2234–2253.

Sánchez-Sesma, F.J. & Vai, R., 1998. Absorbing boundaries in the frequency domain, in *The effect of Surface Geology on Seismic Motion. Recent Progress and New Horizon on EGS Study,* Vol. 2, pp. 961–966, eds Irikura, K., Kudo, K., Okada, H. & Sasatani, T. A.A. Balkema, Rotterdam.

Sato, H. & Fehler, M., 1998. *Seismic Wave Propagation and Scattering in Heterogeneous Earth,* Springer-Verlag, New York.
Shanonn, C.E., 1948. A mathematical theory of communication, *Bell Syst. Tech. J.,* **27,** 379–623.
Strang, G., 1999. The discrete cosine transform, *SIAM Rev.,* **41,** 135–147.
Strang, G. & Fix, G.J., 1973., *An analysis of the Finite Element Method,* p. 306, Prentice Hall, New York.
Thomson. W.T., 1950. Transmission of elastic waves through a stratified solid medium, *J. Appl. Phys.,* **21,** 89–93.
Varadan, V.K., Ma, Y. & Varadan, V.V., 1989. Scattering and attenuation of elastic waves in random media, *Pure appl. Geophys.,* **131,** 577–603.
Virieux, J., 1984. *SH*-wave propagation in heterogeneous media: velocity–stress finite-difference method, *Geophysics,* **49,** 1933–1942.
Yomogida, H., Aki, K. & Benites, R., 1997. Coda *Q* in two-layer random media, *Geophys. J. Int.,* **128,** 425–433.

APPENDIX: ABSORBING BOUNDARY CONDITIONS AND THE WEBER–SCHAFHEITLIN INTEGRAL

For a given wavenumber $k_x \in]-\infty, +\infty[$ the general solution for the wave equation in a homogeneous isotropic medium for the *SH* case is of the form

$$v(x, z, t) = \left[A e^{ik_z z} + B e^{-ik_z z}\right] e^{-ik_x x} e^{+i\omega t}, \tag{A1}$$

where A and B are constants and k_z and k_x are the vertical and horizontal wavenumbers related to the characteristic equation $k_x^2 + k_z^2 = \omega^2/\beta^2$. When z is positive downgoing, the first term in eq. (A1) corresponds to upgoing and the second term corresponds to downgoing waves. In order to ensure absorption at the lower boundaries, Geller & Ohminato (1994) proposed to cancel upgoing waves by imposing the following condition:

$$\frac{dv}{dz} = -ik_z v. \tag{A2}$$

For the general case of a laterally heterogeneous medium, the wavefield in terms of plane waves is given by

$$v(x, z_N) = \sum_l A_l e^{-ik_x^l x}, \tag{A3}$$

where $k_x^l = l\pi/x_N$ and A_l is the amplitude of each plane wave component. The proposed absorbing boundary condition is

$$\frac{\partial v}{\partial z} = \sum_l \left[-ik_z^l A_l e^{-ik_x^l x}\right]. \tag{A4}$$

In Geller & Ohminato (1994) the horizontal dependence of the trial functions is given in terms of plane waves. The result can be extended to the case of trial functions which do not have their horizontal dependency given by plane waves. Since the purpose of this paper is to use cosine basis functions as trial functions we need to prove that the result holds for the more general case. Consider the plane wave given in eq. (2), where k_x is the horizontal wavenumber and $k_z = \sqrt{\omega^2/\beta^2 - k_x^2}$ is the vertical wavenumber. The partial derivative of eq. (2) with respect to z is given by eq. (A2). Note that in the frequency–wavenumber (ω, k) spectral domain the absorbing boundary condition is given by simply multiplying eq. (2) by $-ik_z$. Now consider the upper half-space with normal $\mathbf{n}^{\mathrm{T}} = (n_x, n_z) = (0, 1)$, then the traction on the boundary is

$$t_y(x; \omega, k_x) = \mu \frac{\partial v}{\partial z} = -i\mu k_z v, \tag{A5}$$

where $\mu = \rho\beta^2$ is the shear elastic modulus, ρ is the density of the medium, and $\mathrm{Im}(k_z) \geq 0$. Eq. (A5) can be rewritten as

$$t_y = K v. \tag{A6}$$

This shows the relationship between the surface traction and displacement. In many engineering applications the operator K in eq. (A6) is called the stiffness matrix. Following Kausel (1992), we interpret this condition as the mechanical equivalent of the absorbing condition, and define the stiffness as

$$K(\omega; k_x) = -i\mu k_z = K_R(\omega; k_x) + i K_I(\omega; k_x). \tag{A7}$$

Using the Fourier transform it is possible to write the stiffness matrix in the frequency-space (ω, x) spectral domain as

$$K(\omega; x) = \frac{1}{2\pi} \int_{-\infty}^{+\infty} K(\omega; k_x) e^{+ik_x x} dk_x. \tag{A8}$$

Let $v(\omega, x) = e^{-ik_x x}$, then the traction t_y in the spectral domain (ω, x) is

$$\begin{aligned} t_y(\omega; x) &= \int_{-\infty}^{+\infty} K(\omega; x - \xi) v(\omega, \xi)\, d\xi \\ &= \int_{-\infty}^{+\infty} K(\omega; \xi) v(\omega, x - \xi)\, d\xi \\ &= e^{-ik_x x} \int_{-\infty}^{+\infty} K(\omega; \xi) e^{ik_x \xi}. \end{aligned} \tag{A9}$$

Considering the symmetry of $K(\omega, \xi)$ with respect to ξ, the last integral in eq. (A9) can be written as

$$\begin{aligned} &\int_{-\infty}^{+\infty} K(\omega; \xi) \cos(k_0 \xi) \\ &= \int_{-\infty}^{+\infty} [K_R(\omega, \xi) + i K_I(\omega, \xi)] \cos(k_0 \xi) = \mu i k_z \end{aligned} \tag{A10}$$

in which the discontinuous behaviour of both the real and imaginary parts of the stiffness integral is clear.

In the frequency-space spectral domain, eq. (A6) is transformed into a spatial convolution that gives the traction at a given point in terms of *all* boundary values. Except for the constant μ, eq. (A9) also gives the DtN operator.

Following the analysis of Sánchez-Sesma & Vai (1998), the imaginary part of the stiffness matrix in the spectral domain (ω, x) is given by

$$\begin{aligned} K_I(\omega; x) &= -\frac{1}{2\pi} \int_{-\omega/2}^{\omega/2} \mu \frac{\omega}{\beta} \sqrt{1 - \frac{k_x^2}{\omega^2/\beta^2}} e^{+ik_x x}\, dk_x \\ &= -\frac{1}{2} \omega\rho\beta \frac{J_1(\omega|x|/\beta)}{|x|}, \end{aligned} \tag{A11}$$

where $J_1(\cdot)$ is the Bessel function of the first kind and order one.

In order to compute the traction (A9) for the spectral domain (ω, x), consider the imaginary part of eq. (A10)

$$\begin{aligned} &\int_{-\infty}^{+\infty} K_I(\omega; \xi) \cos(k_0 \xi)\, d\xi \\ &= \begin{cases} \mu \sqrt{\omega^2/\beta^2 - k_0^2}\, v_0(\omega) \cos(k_0 x), & |k_0| < |\omega/\beta| \\ 0, & |k_0| \geq |\omega/\beta|. \end{cases} \end{aligned} \tag{A12}$$

This result is a special case of the Weber–Schafheitlin integrals (Abramowitz & Stegun 1970) [11.4.40].

For the real part of the stiffness matrix K_R we have

$$K_R(\omega; x) = \frac{\mu}{\pi} \int_{\omega/\beta}^{\infty} \sqrt{k_x^2 - \frac{\omega^2}{\beta^2}} \cos(k_x x)\, dk_x. \tag{A13}$$

This leads to the identity

$$\int_{-\infty}^{+\infty} K_R(\omega;\xi)\cos(k_0\xi)\,d\xi = \begin{cases} 0, & |k_0| \le |\omega/\beta| \\ \mu\sqrt{k_0^2-\omega^2/\beta^2}\,v_0(\omega)\cos(k_0 x), & |k_0| > |\omega/\beta|, \end{cases} \tag{A14}$$

which is the real counterpart of eq. (A12). The integrals in eqs (A12) and (A14) may seem straightforward as they reproduce the tractions for harmonic plane waves. However, subtleties have to be addressed: homogeneous plane waves are accounted for entirely by the imaginary part of the stiffness, while the real part is related to inhomogeneous waves. In the frequency-space domain these waves are a mathematical artefact related to the Cartesian reference system. However, in some cases, the free-surface and interfaces induce surface waves with significant participation of inhomogeneous waves. This structure also explains why viscous dampers are used with success in various problems for which it is reasonable to accept that almost all diffracted waves are homogeneous plane waves.